

Simulating 3D Z_2 Topological Nodes in Nonsymmorphic Photonic Crystals

Hai-Xiao Wang,^{1,*} Yige Chen,^{2,*} Zhi Hong Hang,¹ Huanyang Chen,¹ Hae-Young Kee,^{2,3,†} and Jian-Hua Jiang^{1,‡}

¹*College of Physics, Optoelectronics and Energy,
& Collaborative Innovation Center of Suzhou Nano Science and Technology,
Soochow University, 1 Shizi Street, Suzhou 215006, China*

²*Department of Physics, University of Toronto, Toronto, M5S 1A7, Canada*

³*Canadian Institute for Advanced Research, Toronto, Ontario, M5G 1Z8, Canada*

(Dated: September 3, 2022)

We propose an all-dielectric, space-time reversal symmetric photonics-crystal architecture that possess 3D Dirac points and line-nodes with nontrivial Z_2 topological charge, which can be realized at infrared and microwave frequencies. The protected degeneracy of bands is achieved via nonsymmorphic symmetries despite the lack of Kramers degeneracy in photonic crystal systems. Two orthogonal screw axes lead to 3D Z_2 Dirac points on high symmetry Brillouin zone (BZ) boundary line. On the other hand, twofold Z_2 line-nodes appear around the Γ -point due to a combination of nonsymmorphic and point-group symmetries. The lowest line-node is deterministic because of degeneracy partner switching between Bloch states with opposite parities. A pair of Fermi arcs associated with Z_2 topological charge is emerged below light-line and protected by total internal reflection on certain photonic-crystal-air interfaces. These robust surface states offer an unique opportunity to realize “open cavity” with strong interaction between quantum emitters and engineered vacuum with nontrivial topology — an important step toward symmetry-protected topological states in interacting bosonic systems. Realistic calculation yields very large vacuum Rabi splitting reaching to 20% of the oscillator frequency, when optical phonons in boron nitride thin film are coupled resonantly with the cavity photons. We also show that type-II Dirac cones have valley selective excitation which depends only on the direction of incident light, opening a route to valley physics in Dirac photonic systems.

PACS numbers: 42.70.Qs, 78.67.Pt, 03.65.Vf

I. INTRODUCTION

The study of topological properties of energy bands lies at the heart of frontiers of condensed matter physics, ranging from topological insulators[1, 2], topological superconductors[2], topological semimetals[3–5] and symmetry-protected topological states in strongly correlated quantum materials[6, 7]. Recent discoveries of Dirac and Weyl semimetals with ultrahigh mobility and other exotic properties bring those developments closer to material science and applications.

In parallel, photonics is another realm where achieving robust transport[8–11], selective waveguiding[12], and manipulation of angular momentum[13] is of central importance. These are the major challenges in photonic circuits, metamaterials, and quantum optics. Photonic topological states introduce new routes to overcome those challenges. For instance, back-scattering immune edge states of photonic quantum Hall systems are perfect solution for robust and unidirectional waveguiding[14–17]. Recent developments on manipulation of light propagation via polarization and angular momentum request strong spin-orbit coupling and strong angular-momentum–wavevector correlation[13]. These properties are available from topological nodes in photonic

bands[18–24]. Right at the heart of photonic topological states, there are nontrivial Berry phases as well as robust surfaces states[25, 26], which offer unprecedented control of light flows[14, 17, 27–30].

In this work, we propose to simulate 3D Z_2 topological Dirac points and line-nodes in nonsymmorphic *all-dielectric* photonic crystals (PhCs) with space-time reversal symmetry. We focus on Z_2 topological Dirac points (fourfold point-degeneracy) and Z_2 line-nodes (twofold line-degeneracy), their topological surface states, and applications. All-dielectric PhCs can be fabricated with well-controlled geometries for microwave to near-infrared frequencies. Disorder and interaction effects that complicate the band structure of electrons can be diminished in photonic bands. Compared with metamaterials or magneto-optical materials[19, 22], all-dielectric PhCs are lossless materials that preserve the coherence of photon at large-scales and long-times. Future developments of topological photonics will benefit from simple all-dielectric PhCs without using lossy magneto-optical materials or metamaterials, where photonic Z_2 topology becomes very important[21, 23].

However, since photon is boson which does not have Kramers degeneracy, it is challenging to create Z_2 topological states in all-dielectric PhCs[21, 23]. Up till now, there are very few studies on 3D Z_2 topological states in PhCs, based on magneto-optical materials[31] or point group symmetry[23]. In this work, we show that photonic Z_2 topological states can be created using nonsymmorphic symmetry. Specifically, screw symmetries gen-

* These authors contributed equally

† hykee@physics.utoronto.ca

‡ jianhua.jiang@suda.edu.cn

erate twofold degeneracy for all states on certain high symmetry planes of the BZ. This mechanism, similar to Kramers degeneracy in fermionic systems, leads to rich phenomena in band degeneracy and degenerate partner switching. As a consequence, a number of 3D Z_2 Dirac points and Z_2 line-nodes are created, unveiling effective methodology toward photonic Z_2 topological states.

Furthermore, we found the ‘‘Fermi arcs’’ associated with the Z_2 Dirac points, revealing that the surface states are a pair of mirror symmetric, helically dispersed bands with opposite helicity. These robust, double helicoid surface states can be observed in microwave experiments readily. We further show that part of the surface states survive on the (100) and (010) interfaces between the photonic crystal and air, since they emerge below the light-line. Similar confinement of surface states associated with Z_2 line-nodes appear on the (001) interface. Such surface states offer access to ‘‘open cavity’’ states with nontrivial Berry phases. Placing hexagonal boron-nitride multilayers brings in *ultrastrong* light-matter interaction with vacuum Rabi splitting reaching to 20% of the optical phonon frequency which is induced by significant enhancement of electromagnetic fields at the interface. This offers a useful route towards ultrastrong coupling regime where the quantum nature of photon becomes significant[32–37]. In addition, this scheme opens the possibility toward simulation of quantum bosonic systems with both nontrivial Berry phase as well as strong interaction, where symmetry-protected topological states of interacting photons may emerge[7]. Moreover, we find that type-II Z_2 Dirac points can be exploited as effective medium for the study of valley physics, where the valley selective excitation occurs depending on the direction of incident light.

II. NONSYMMORPHIC ALL-DIELECTRIC PHOTONIC CRYSTALS

To demonstrate creation of topological nodes using nonsymmorphic symmetries, we study a simple all-dielectric PhC of which the structure is illustrated in Figs. 1(a), 1(b), and 1(c). It is tetragonal lattice with space group of $P4_2/mcm$. In each unit cell (with lattice constant a along all three directions) there are two orthogonal dielectric blocks (painted as yellow and green) of the same shape that are embedded in the background medium. Each block has length $l = 0.5a$, width $w = 0.2a$, and height $h = 0.5a$, separately. The centers of the blocks are at $(0, 0, 0)$ and $(0.5a, 0.5a, 0.5a)$, respectively (origin of the coordinate is defined as the center of the unit cell). The blocks have (relative) permittivity $\varepsilon_s = 24$, while the background medium has permittivity $\varepsilon_b = 2.2$. The blocks can be made of high-index materials such as tellurium (for wavelength longer than $4 \mu\text{m}$), whereas the background material can be polymers such as PMMA.

The tetragonal lattice PhC possesses the following el-

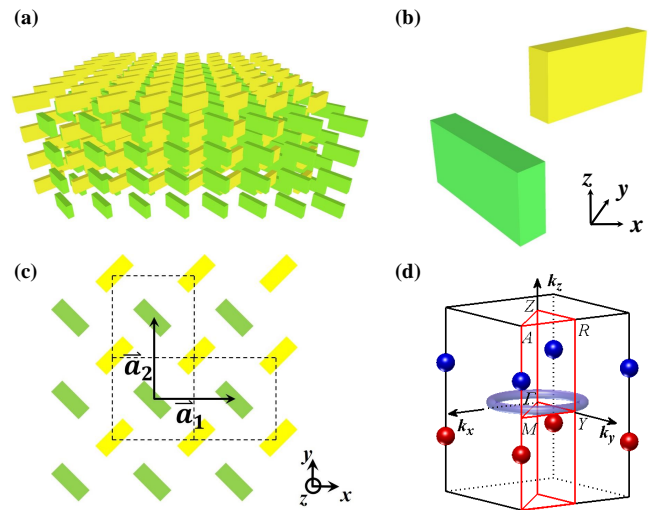


FIG. 1. (Color online) (a) Tetragonal lattice photonic crystal with nonsymmorphic symmetries. (b) Structure of a real space unit cell. (c) Top-down view of the photonic crystal. Yellow and green blocks are of the same material and shape. Nonsymmorphic symmetry operations are geometrical transformations that transform between the yellow and the green blocks. \vec{a}_1 and \vec{a}_2 are the lattice vectors in the x - y plane. $|\vec{a}_1| = |\vec{a}_2| = a$. (d) First BZ with a pair of Dirac points at the M - A line and line-nodes around the Γ point in the $k_z = 0$ plane.

emental symmetries,

$$\begin{aligned} \mathcal{P} &: (x, y, z) \rightarrow (-x, -y, -z), \\ M_1 &: (x, y, z) \rightarrow (y, x, z), \\ M_2 &: (x, y, z) \rightarrow (-y, -x, z), \\ G_x &: (x, y, z) \rightarrow (0.5a - x, 0.5a + y, 0.5a + z). \end{aligned} \quad (1)$$

and their combinations. For instance, there are two screw symmetries and another glide symmetry,

$$G_y = G_x C_{2z}, \quad S_x = G_x \mathcal{P}, \quad S_y = G_y \mathcal{P}. \quad (2)$$

It is important to define the 180° rotation along z axis

$$C_{2z} \equiv M_1 M_2 : (x, y, z) \rightarrow (-x, -y, z), \quad (3)$$

and mirror symmetry with respect to the $z = 0$ plane,

$$M_z \equiv \mathcal{P} C_{2z} : (x, y, z) \rightarrow (x, y, -z). \quad (4)$$

The nonsymmorphic symmetries transform the yellow blocks into green blocks (and vice versa), while the symmorphic symmetries transform within each type of blocks. In PhCs, since for the same band the Bloch functions of the electric field and the magnetic field carry the same symmetry information, we will use only the magnetic fields \vec{h} for the discussions on the symmetries of photonic bands henceforth. The magnetic field is a pseudovector which is even under space inversion but odd under time-reversal operation. Therefore, the explicit form

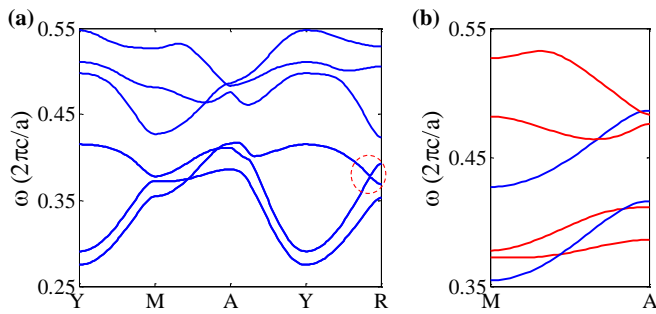


FIG. 2. (Color online) (a) Band structure for the $k_y = \frac{\pi}{a}$ plane. The dashed red circle contains an anti-crossing of two sets of doubly degenerate bands. (b) Band dispersion along the M - A line. In this line, the photonic bands are eigen functions of the 180° rotation around the M - A line, the c_{2z} operator. The eigenvalues can be -1 (odd parity) or 1 (even parity), as labeled by red and blue in (b), respectively. Crossing of bands with opposite parity yields Dirac points. Bands of the same parity avoid crossing.

of time-reversal operator for the magnetic field is $-\mathcal{K}$ where \mathcal{K} is the complex conjugation operator. However, we shall shortly denote the time-reversal operator as

$$\mathcal{T} : t \rightarrow -t. \quad (5)$$

The apparent parities (i.e., mirror symmetries) of the magnetic fields are also useful for constructing the $\vec{k} \cdot \vec{P}$ theory of photonic bands around the topological nodes [see Appendix A].

Since both time-reversal and inversion symmetry exist, the $U(1)$ Berry phase vanishes. There can only be $SU(2)$ Berry phase and Z_2 topological orders. For topological nodes, there can only be Z_2 Dirac points and Z_2 line-nodes, whereas Weyl points cannot emerge in our PhC (unless inversion symmetry is broken).

III. Z_2 TOPOLOGICAL NODES IN BULK BANDS

A. Band degeneracy from screw symmetries

We now show that nonsymmorphic symmetries are effective tools for generation of double degeneracy in all-dielectric PhCs. In our PhCs, the double degeneracy's are induced by the following two *anti-unitary* symmetry operators:

$$\begin{aligned} \Theta_x &\equiv S_x \mathcal{T} : (x, y, z, t) \rightarrow \\ &\quad (0.5a + x, 0.5a - y, 0.5a - z, -t), \\ \Theta_y &\equiv S_y \mathcal{T} : (x, y, z, t) \rightarrow \\ &\quad (0.5a - x, 0.5a + y, 0.5a - z, -t), \end{aligned} \quad (6)$$

where S_x and S_y are the screw operations defined in Eq. (2). It's straightforward to show that for all Bloch states, of the form $\Psi_{n\vec{k}}(\vec{r}) = e^{i\vec{k} \cdot \vec{r}} u_{n\vec{k}}(\vec{r})$ (u_n can be a vector, is a periodic function of lattice translation while n is the band index),

$$\Theta_x^2 \Psi_{n\vec{k}}(\vec{r}) = e^{-ik_x a} \Psi_{n\vec{k}}(\vec{r}). \quad (7)$$

The Θ_x operator transform (k_x, k_y, k_z) to $(-k_x, k_y, k_z)$. Therefore, for the $k_x = \frac{\pi}{a}$ plane (which is invariant under Θ_x), $\Theta_x^2 = -1$ dictates twofold degeneracy similar to the Kramers degeneracy for spin-1/2 electronic systems. Similarly, for the $k_y = \frac{\pi}{a}$ plane, *all* Bloch states are doubly degenerate due to $\Theta_y^2 = -1$. In fact, due to the M_1 mirror symmetry, the spectrum is same for the $k_y = \frac{\pi}{a}$ plane as for the $k_x = \frac{\pi}{a}$ plane. The band structure for the $k_y = \frac{\pi}{a}$ plane is shown in Fig. 2(a). Away from the $k_y = \frac{\pi}{a}$ plane, the twofold degeneracy is lifted due to \vec{k} -linear coupling between the bands (see Appendix A for reference). The special properties of the Θ_x operator, originating from the screw symmetry S_x , reveal that nonsymmorphic symmetry plays an important role in photonic Z_2 topological orders. Away from the $k_y = \frac{\pi}{a}$ or $k_x = \frac{\pi}{a}$ plane, the twofold band degeneracy is split and $SU(2)$ Berry phases are generated by interaction between these bands.

B. Dirac points on M - A line

Dirac points are fourfold degenerate points with linear-dispersion where the effective Hamiltonian describing the photonic states resembles that of massless Dirac equation [The effective Hamiltonian can be obtained via $\vec{k} \cdot \vec{P}$ expansion of the Maxwell equation around the Dirac point (see Appendix A)]. A Dirac point has vanishing Chern number but may carry nontrivial Z_2 topology. The topological charge of Dirac points can be determined through its low-energy Hamiltonian. In simple situations, it can be determined by the eigenvalues of the rotation symmetry that protects the Dirac points[38]. Z_2 topological Dirac points appear in pairs (at two \vec{k} points linked by time-reversal operation) with *opposite* Z_2 topological charge.

The two planes $k_x = \frac{\pi}{a}$ and $k_y = \frac{\pi}{a}$ share a common line, i.e., the M - A line: $(\frac{\pi}{a}, \frac{\pi}{a}, k_z)$, $\forall k_z$. We show that in this high-symmetry line Dirac points can emerge as accidental fourfold degenerate points as shown in Fig. 2(b). It is crucial to notice that

$$\Theta_y \Theta_x = e^{-i(k_x + k_y)a} \Theta_x \Theta_y. \quad (8)$$

Therefore, Θ_x commute with Θ_y on the M - A line. In addition, on this line C_{2z} is a symmetry operation and

$$\Theta_x \Theta_y = e^{-ik_x a} C_{2z} \Big|_{k_x a = \pi} = -C_{2z}. \quad (9)$$

Therefore, C_{2z} commutes with both Θ_x and Θ_y . As a consequence, each doublet (i.e., $\Psi_{n\vec{k}}(\vec{r})$ and $\Theta_x \Psi_{n\vec{k}}(\vec{r})$)

has the same C_{2z} eigenvalue (denoted as c_{2z}). Since C_{2z} is 180° rotation around z axis, its eigenvalue $c_{2z} = \pm 1$ gives the parity for each doublet. When two doublets with opposite parity crossing each other on the M - A line, there will be no interaction between them since they carry different C_{2z} eigenvalues. Such a band crossing is then a Dirac point, which is protected by the C_{2z} operator. The Z_2 topological charge measures the parity inversion across the the Dirac point. According to Ref. [38], the Z_2 topological charge of a Dirac point at $(\frac{\pi}{a}, \frac{\pi}{a}, k_{DP})$ is given by

$$\mathcal{N}_{DP} = \frac{1}{2}[c_{2z}^-(k_{DP}^+) - c_{2z}^-(k_{DP}^-)] \quad (10)$$

where $k_{DP}^+ = k_{DP} + 0^+$ and $k_{DP}^- = k_{DP} - 0^+$ are the wavevectors slightly larger or smaller than k_{DP} , respectively. Here c_{2z}^- denotes the C_{2z} eigenvalue of the lower doublet near the Dirac point. Therefore, a Dirac point is a source or drain of parity inversion. For our PhCs, there are several Dirac points along the M - A line. The parity of those bands are labeled by colors in Fig. 2(b). If $c_{2z} = -1$ (i.e., odd parity) then it is labeled as red. If $c_{2z} = 1$ (i.e., even parity) then the band is labeled as blue. We find that the lowest four Dirac points with $k_z > 0$ all carry topological charge $\mathcal{N}_{DP} = -1$, while the lowest four Dirac points with $k_z < 0$ all carry topological charge $\mathcal{N}_{DP} = 1$. This configuration leads to topological surface states around $k_y = \frac{\pi}{a}$ and $k_z = 0$ for (100) surface.

We remark that the above scenario does not apply for the X - R line ($k_x = \pi/a, k_y = 0$) or the Y - R' line ($k_x = 0, k_y = \pi/a$). On these lines, according to Eq. (8), Θ_x anti-commutes with Θ_y since $k_x + k_y = \pi/a$. The degenerate partners in each doublet then have opposite c_{2z} . Hence the two sets of doubly degenerate bands cannot crossing each other without interaction. In fact, we observe anti-crossing on the X - R and Y - R' lines.

We notice from Fig. 2 that there are both type-I and type-II Dirac cones. The first three Dirac points are type-II Dirac points, while the fourth Dirac point is of type-I. To explore the properties of these Dirac points, we plot their dispersion on the k_y - k_z plane in Figs. 3(a) and 3(b). Fig. 3(a) is for the fourth Dirac point, while Fig. 3(b) is for the second Dirac point. Fig. 3(a) shows a Dirac cone with slightly tilt dispersion. In comparison, Fig. 3(b) shows a highly tilted Dirac cone. The difference between the two Dirac cones is further displayed in Figs. 3(c) and 3(d). Fig. 3(c) shows that type-I Dirac point has closed isofrequency contours. Approaching the Dirac point the circumference of the isofrequency surface tends to zero. In contrast, type-II Dirac cones, as shown in Fig. 3(d), exhibits open isofrequency contours consisting of two unconnected branches. In approaching the frequency of the Dirac point, the two branches touch each other at the Dirac point. Therefore, the density of states can be much greater for type-II Dirac points which may lead to enhanced light-matter interaction. We shall show in Sec. VI B that type-II Dirac points lead to anomalous

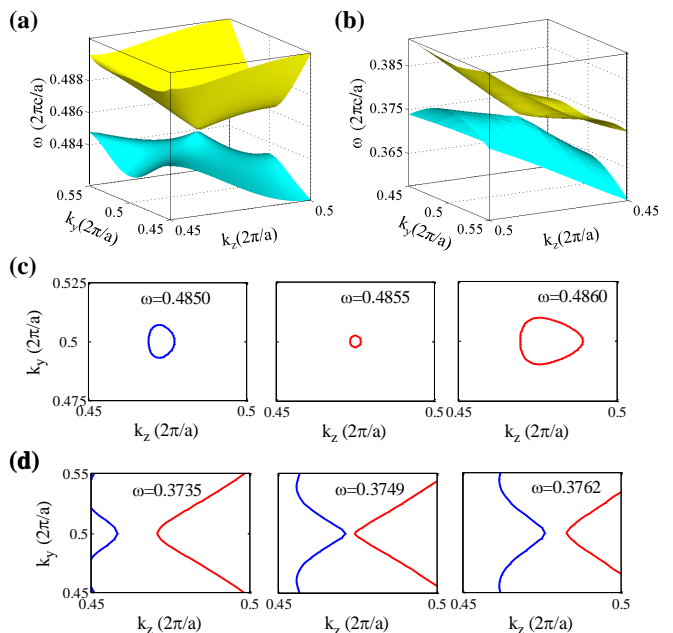


FIG. 3. (Color online) Photonic dispersion around a (a) type-I and (b) type-II Dirac point in the k_y - k_z plane. The type-I Dirac point is the fourth Dirac point, while the type-II Dirac point is the second Dirac point, counting from low to high frequency. Isofrequency contour of the (c) type-I and (d) type-II Dirac cone.

refraction and valley selective excitation.

IV. Z_2 LINE-NODES AROUND Γ POINT

A Z_2 line-node is a line degeneracy at each point on the line there is a linear crossing through which the parity of the Bloch states is interchanged. Since a line-node is a time-reversal invariant object (it includes both a degenerate \vec{k} point and its time-reversal partner $-\vec{k}$), line-nodes do not have to appear in pairs. Line-nodes in our PhC are protected by a mirror symmetry as well as by the nonsymmorphic glide symmetries as elaborated below. The Z_2 topological charge of a line-node is then defined as

$$\mathcal{N}_{LN} = \frac{1}{2}(m_i - m_o). \quad (11)$$

Here m_i and m_o denote the eigenvalues of the mirror symmetry that protects the line-node for \vec{k} inside and outside the line-node, respectively. They are calculated for the band with lower frequency. \mathcal{N}_{LN} can be ± 1 if it is topologically nontrivial.

In our PhC line-nodes appear as a consequence of the coaction of the nonsymmorphic and symmorphic symmetries. The line-nodes are on the $k_z = 0$ plane. The only crystal symmetry is invariant on this plane is M_z . Furthermore, M_z commute with both Θ_x and Θ_y when $k_z = 0$. Hence, $(|m_z\rangle)$ labels a Bloch state which is an

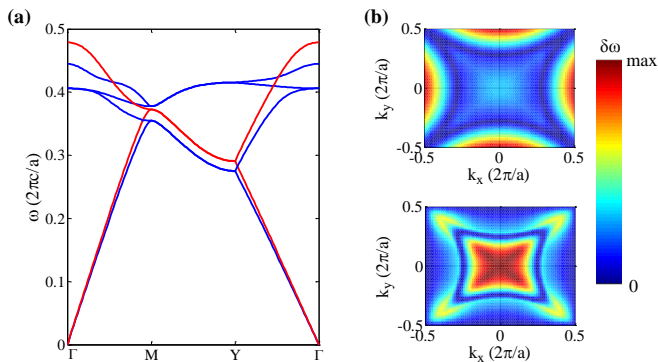


FIG. 4. (Color online) (a) Photonic band structure for $k_z = 0$ plane. Red curves label bands with $M_z = -1$, while blue curves label bands with $m_z = 1$. (b) Upper: frequency difference between the fourth band and the fifth band; Lower: frequency difference between the fifth band and the sixth band in the $k_z = 0$ plane.

eigenstate of the M_z operator with eigenvalue m_z)

$$M_z \Theta_i |m_z\rangle = \Theta_i M_z |m_z\rangle = m_z \Theta_i |m_z\rangle, \quad (12)$$

for $i = x, y$. The above equation indicates that the degenerate partners, $|m_z\rangle$ and $\Theta_x |m_z\rangle$, at the X - M line has the *same* M_z eigenvalue. Similarly, the two degenerate states $|m_z\rangle$ and $\Theta_y |m_z\rangle$ at the Y - M line has the *same* M_z eigenvalue. Due to the intrinsic property of Maxwell equations, in the long wavelength limit $\lambda \gg a$, the bands become TM and TE modes which have opposite M_z eigenvalues. The two modes become degenerate in the zero frequency limit. When such degenerate bands with *opposite* M_z eigenvalues evolve to some generic point on the X - M or Y - M line and then evolve back to the Γ point, there must be at least one crossing of bands with opposite M_z eigenvalues [see Fig. 4(a)]. Such degenerate partner switching between bands with opposite M_z eigenvalues leads to a *deterministic* line-node. Here the deterministic line-node is the lowest line-node. Higher line-nodes can in principle be removed by continuously tuning the bands. The lowest line-node is then protected by the mirror symmetry M_z as well as the nonsymmorphic symmetries Θ_x and Θ_y .

Higher line-nodes can be understood through the nature of degeneracy for higher bands at Γ point. At Γ point, all nonsymmorphic symmetries are degraded to symmorphic symmetries, since translation has no effect on Bloch states at $\vec{k} = 0$. The symmetry of Bloch states is the same as if the two orthogonal blocks are sitting together with their centers overlap at the center of the unit cell. The whole symmetry group for the Bloch states is then equivalent to $C_{4v} \otimes M_z$. The degeneracy at Γ point is then determined by this point group. For instance, the third and fourth bands are degenerate due to the C_{4v} point group. The two bands are of the same M_z eigenvalue ($m_z = 1$) and of p -wave nature in the x - y plane. The fifth band is also of $m_z = 1$, however, it is of d -

wave nature in the x - y plane. This is consistent with the physics picture that the even-parity modes have lower frequency. As a consequence, there emerge another two line-nodes as the odd parity band crossing the other two even parity bands [see Fig. 4(a)]. To confirm that these crossings are indeed line-nodes, we plot the frequency difference between the fourth and fifth bands, as well as that between the fifth and sixth bands in the $k_z = 0$ plane in Fig. 4(b). We find that the fourth and fifth bands, in fact, form four line-nodes that are unable to contract to a point, since they circulate the BZ at $k_z = 0$ several times. On the other hand, the fifth and sixth bands form a line-node that can contract to a point.

V. TOPOLOGICAL SURFACE STATES

The surface states associated with the topological nodes is governed by the projection principle. The topological nodes projected onto the surface BZ act as source or drain of the surface states, depending on its topological charge. For example, a pair of Weyl points with opposite Chern number lead to helically dispersed surface states, according to the bulk-edge correspondence principle[28, 39]. A pair of Z_2 Dirac points lead to two helical surface states with opposite helicity[40, 41], due to the same principle. In such a pair of Z_2 Dirac points, the Dirac point with charge $+1$ acts as source of Z_2 topology (or “monopole” of $SU(2)$ Berry fluxes with charge $+1$), whereas the other Dirac point with charge -1 acts as the drain of Z_2 topology. Hence, if the two Dirac points are projected into the same \vec{k} point on the surface BZ, there will be no surface states. Note that topological degeneracy’s with opposite Z_2 charge are linked by time-reversal symmetry, i.e., they are of opposite wavevectors. According to the projection principle, the (100) and (010) surface states are associated with the Z_2 Dirac points, whereas the (001) surface states are associated with the Z_2 line-nodes.

A. Double helicoid surface states on (100) surface associated with Z_2 Dirac points

We calculate the edge states on the (100) surface of our photonic crystal for a supercell stacking along x direction (for details see Appendix B). The screw symmetry S_y , which is essential for double degeneracy at $k_y = \frac{\pi}{a}$, is kept for the supercell. The surface BZ is shown in Fig. 5(a). There are two helical surface states with opposite helicity in the surface BZ. Their spectra transform into each other under $\Theta_y : (k_y, k_z) \rightarrow (-k_y, k_z)$. The Θ_y symmetry ensures that the spectrum of the surface states are “mirror symmetric”. In addition, time reversal symmetry ensures that the spectrum is also symmetric under the transformation $(k_y, k_z) \rightarrow (k_y, -k_z)$. Two almost degenerate surface states can be identified in Fig. 5(b). The field profiles in Fig. 5(c) reveal that these two states

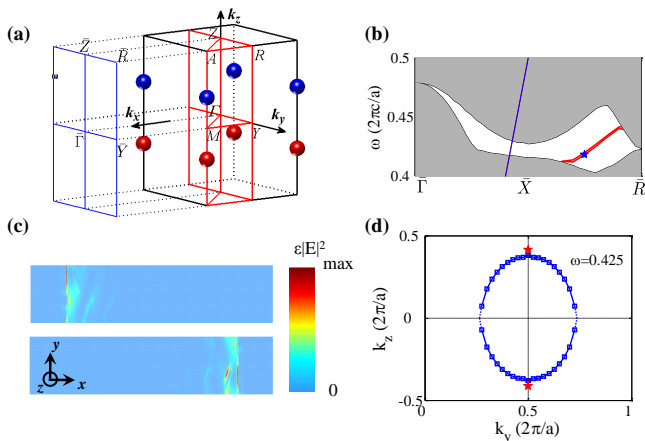


FIG. 5. (Color online) (a) Dirac points and surface Brillouin zone. The red Dirac points have topological charge $\mathcal{N}_{DP} = -1$, while the blue one has $\mathcal{N}_{DP} = 1$. The supercell is stacked along x direction, so that the surface BZ is folded to the k_y - k_z plane. (b) Dispersion of topological surface states (red) as well as projected bulk photonic bands (gray). (c) Electromagnetic energy profiles for the two surface states in the x - y plane. The wavevector of the edge states are given by the star in (b). (d) Double “Fermi arcs” due to Z_2 Dirac points (labeled as red stars on the $k_y = \pi/a$ line).

are edge states at opposite surfaces. To make sure that these are topological edge states, we compute the “Fermi arcs” through a scan of the edge states in the surface BZ. The “Fermi arcs” at frequency $0.425 \frac{2\pi c}{a}$ (c is the speed of light in vacuum). The Fermi arcs associated with the Z_2 Dirac points are plotted in Fig. 5(d). From the figure we find that the two helical surface states intersect with each other on the $k_y = \frac{\pi}{a}$ line where they become degenerate, as protected by Θ_y . The two Dirac points are projected onto the $k_y = \frac{\pi}{a}$ line as well [indicated by red points in Fig. 5(d)]. The mirror symmetric Fermi arcs is a smoking-gun signature of the topological nature of the surface states. The double degeneracy due to $\Theta_y^2 = -1$ ensures that the two helical surface states do not interact with each other at $k_y = \frac{\pi}{a}$. Such double helicoid edge states is hence robust as protected by the Θ_y symmetry. Similar surface states were found in a recent work in electronic materials with quite different symmetry[41]. The surface states are found to be quite robust to surface truncation geometries (see Appendix C), demonstrating topological protection.

B. (001) surface states associated with Z_2 line-nodes

The topological charge of each line-node is defined by Eq. (11). We find that the lowest line-node is of $\mathcal{N}_{LN} = -1$, whereas the second and third line-nodes have topological charge $\mathcal{N}_{LN} = 1$. The bulk topology dictates that there is surface states on the (001) surface. We re-

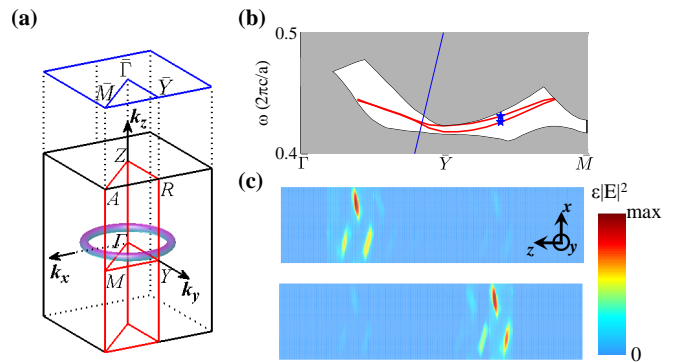


FIG. 6. (Color online) (a) Line-nodes and surface Brillouin zone. (b) Spectrum of the edge states (red curves) and projected bulk bands (gray). (c) Electromagnetic energy profiles for the two surface states in the x - z plane.

mark that on (001) surface the Z_2 Dirac points have no effect, since two Dirac points with opposite Z_2 charge project to the same point.

To reveal the topological surface states on the (001) plane, we calculate the spectrum of the surface states using a supercell with 7 periods of our PhC. There are two branches of surface states, each of which is associated with one of the interface [see Figs. 6(b) and 6(c)]. Two nearly degenerate surface states are associated with the left and right surfaces. The small splitting is an artifact of finite size calculation. From the frequency range we judge that the surface states are associated with the third line-node. The first two line-nodes are close to each other and have opposite topological charge. They largely cancel with each other and their effects are not reflected on the surface states. We emphasize that part of the surface states are below the light-line and hence can exist on the PhC-air interfaces for (001) surface.

VI. APPLICATIONS

A. Ultrastrong light-matter interaction at photonic-crystal-air surface

One important application of the Z_2 topological states in our PhCs is to realize an “open cavity” at the interface between PhC and air [see Fig. 6(a)]. There are topological surface states below the light-line [see Figs. 5(b) and 6(b)]. Those surface states are confined at the PhC-air interface without additional light-trapping mechanism. We show that such configuration is highly favorable for strong light-matter interaction as well as for experimental fabrication and measurements. First, since air has lower dielectric constant than a dielectric mirror, the electric field in the air region close to the interface is much enhanced. The electric field profile in Fig. 6(a) illustrate the strong confinement of light at the PhC-air interface. Such strong light focusing can leads to very strong light-

matter interaction which is crucial for the study of quantum nature of photons as well as single-photon quantum optics.

To demonstrate the merits of the surface states, we calculate the interaction between TO-phonon in hexagonal boron-nitride (h-BN) and cavity photon for the situation when a thin film of h-BN is placed on top of the PhC interface. The interacting phonon-photon system is described by the following Hamiltonian,

$$H = \sum_{\vec{k}} [\hbar\omega_{TO}(\vec{k})b_{\vec{k}}^\dagger b_{\vec{k}} + \hbar\omega_{\vec{k}}a_{\vec{k}}^\dagger a_{\vec{k}}] + H_I, \quad (13a)$$

$$H_I = \sum_{\vec{k}} g_{\vec{k}}(b_{\vec{k}}^\dagger a_{\vec{k}} + a_{\vec{k}}^\dagger b_{\vec{k}}), \quad (13b)$$

where $\omega_{TO}(\vec{k})$ is the dispersion of the TO phonon which is almost flat as compared with the photonic dispersion $\omega_{\vec{k}}$ of the surface states. $b_{\vec{k}}^\dagger$ creates a TO phonon in the h-BN thin film with wavevector \vec{k} , whereas $a_{\vec{k}}^\dagger$ creates surface photon in the open cavity. The collective coupling between phonon and photon is calculated as[42, 43]

$$g_{\vec{k}} = \frac{\sqrt{L_c s^2}}{2} \sqrt{\sum_l S_{u.c.}^{-1} \int_{u.c.} dydz |E_p(y, z, x_l)|^2}, \quad (14)$$

where $L_c = 0.47$ nm is the thickness of a single h-BN monolayer, $\hbar\omega_{TO} = 170$ meV is the TO-phonon energy, the coupling coefficient is $s^2 = 3.49 \times 10^{10} (2\pi)^2 c^2 \hbar^2$ (in unit of Joule²) as determined by experimental measurement[44]. The integral here is performed on the strength of the electric field along the y - z plane (i.e., parallel to the h-BN monolayer plane) $|E_p|^2 = |E_y|^2 + |E_z|^2$, since polarization of the TO phonon is along the y - z plane. x_l is the position of the l -th h-BN monolayer. The electric field here is normalized as $S_{u.c.}^{-1} \int_{u.c.} d\vec{\rho} dz \epsilon(\vec{r}) |\vec{E}(\vec{k}, \vec{r})|^2 = 1$ for the surface states.

The interaction g is calculated for $\vec{k} = (0, 0.5, -0.3)\frac{2\pi}{a}$. The dependence of g on the thickness of the h-BN thin film is shown in Fig. 6(c). The interaction increases approximately square root of the thickness of the thin film, since the collective coupling increases with the square root of number of h-BN monolayers. With a h-BN thin film of thickness 400 nm ($\approx 0.13a$), the phonon-photon coupling g reaches to 17 meV. The vacuum Rabi splitting is as large as 20% of the phonon frequency, signifying the *ultrastrong* coupling regime[32]. We have chosen the lattice constant $a = 3 \mu\text{m}$ to ensure that the TO-phonon is in resonance with the edge state.

In quantum optics, when the ratio $g/\hbar\omega_{TO} \geq 0.1$, the system enters into the ultrastrong coupling regime. There are several nontrivial properties of an ultrastrong coupling system. For instance, the ground state of an ultrastrong coupling system has a finite population of bound photons which enables quantum vacuum emission[37]. The ultrastrong coupling system can also be exploited to study strong single photon nonlinearity and quantum phase transition[45]. Nontrivial Berry

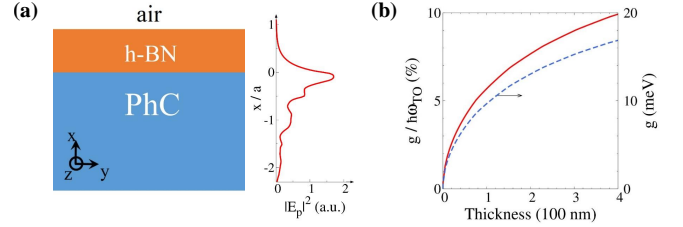


FIG. 7. (Color online) (a) Open cavity at the interface between PhC and air. A thin film of hexagonal boron nitride is placed on top of the PhC. Right panel: distribution of intensity of inplane electric field $a^{-2} \int dydz |E_p(\vec{r})|^2$ over the x direction. Interface between PhC and air is at $x = 0$. (b) Coupling between TO-phonon and photon g . Ratio $g/(\hbar\omega_{TO})$ is calculated for the edge state ($\vec{k} = (0, 0.5, -0.3)\frac{2\pi}{a}$) in resonance with TO-phonon for $a = 3 \mu\text{m}$. TO-phonon has energy $\hbar\omega_{TO} = 170$ meV in hexagonal boron nitride.

phases and strong interaction are two key elements of interacting symmetry-protected topological states. Such interaction-driven bosonic topological states have been constructed recently[7]. However, it is rather challenging to realize such states in known physical systems. Our system with phonon-polaritons in the ultrastrong coupling regime might open a route to such states since both strong interaction and nontrivial Berry phases exist in our system. Future studies should address the relevant parameter regimes for quantum simulation of strongly interacting topological phonon-polariton gas.

In addition, fabrication of such cavity can be much easier than the sandwich shaped cavity as studied in the literature for both Fabry-Pérot cavities[32, 43] and PhC cavities[42]. The PhC considered here can be fabricated using mature commercial technology such as ©NanoScribe. After that the h-BN thin film can be fabricated separately and transferred to the surface. Moreover, it is easier to study the physical properties of the ultrastrong coupling phonon-photon system on the PhC-air interface. Instruments such as near field scanning can be useful for Hanbury Brown-Twiss interferometry and other high-order photon correlation measurements.

B. Anomalous refraction and valley physics of Z_2 Dirac points

In our PhC, the Dirac points are on the M - A line with $k_x = k_y = \frac{\pi}{a}$. Through a surface 2D grating with periods along both x and y being $2a$, light from air can directly couple to those Dirac points. It is equivalent to regard the effect of the surface grating as duplicating the light cone of air at $\vec{k} = (0, 0, 0)$ to $(\frac{\pi}{a}, \frac{\pi}{a}, 0)$. The refraction of this duplicated light cone through the Dirac points is the focus of study in this section [see Fig. 7(a)]. We will show that type-II Z_2 Dirac cones (i.e., tilted Dirac cones) leads to anomalous refraction and valley physics.

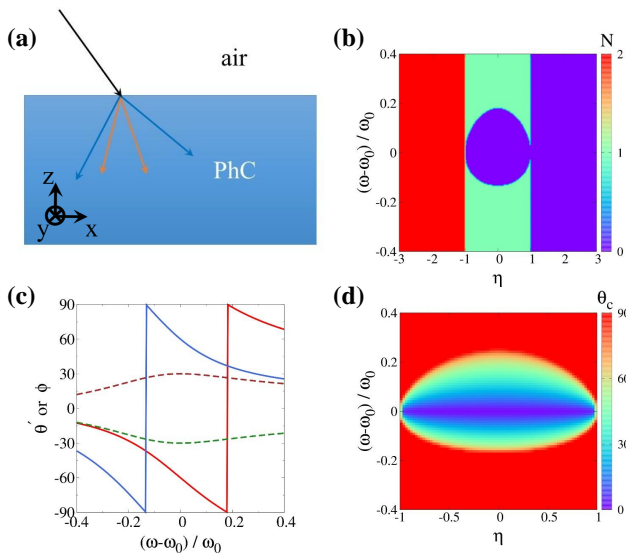


FIG. 8. (Color online) (a) Anomalous refraction through type-II Dirac point. A light beam from air (black arrow) is shed on the PhC, which are refracted into two beams, with different wavevectors (blue arrows) and group velocities (orange arrows). Group velocity of the two beams are the same along z direction but opposite along x direction. (b) Number of refractive beams N for various frequency ω and η when the incident angle is $\theta = 50^\circ$. There are two refractive beams for $\eta < -1$, whereas no refractive beam for $\eta > 1$. (c) The angles for the wavevectors θ' and group velocities ϕ for the two refractive beams in PhC as functions of frequency ω for incident angle $\theta = 50^\circ$ and $\eta = -2$. The red (blue) curve represents θ'_1 (θ'_2), the brown (green) curve represents ϕ_1 (ϕ_2). (d) Critical angle θ_c for type-I Dirac cone vs. frequency and η . Parameters: $\omega_0 = 0.5 \frac{2\pi c}{a}$ and $v = 0.2c$ with c being speed of light in vacuum.

In our PhC the main deformation of Dirac cones comes from a finite velocity along the z direction. Taking into account of such deformation, photonic dispersion around a Dirac point is written as

$$\omega = \omega_0 + v(\eta q_z \pm q). \quad (15)$$

Here ω_0 is the frequency at the Dirac point, v is the group velocity of the Dirac point. The dimensionless parameter η measures the degree of tilt of the Dirac cone along q_z direction. Here $\vec{q} = (q_x, q_y, q_z)$ represents the deviation of the wavevector away from the Dirac point at $(\frac{\pi}{a}, \frac{\pi}{a}, k_{DP})$ and $q = \sqrt{q_x^2 + q_y^2 + q_z^2}$.

The refraction angle is determined by the frequency ω and incident angle θ of the light. Since the dispersion is isotropic in the q_x - q_y plane, we can simplify the problem by setting $q_y = 0$. The conservation of frequency and q_x determines the refraction angle θ' ,

$$\begin{aligned} \omega - \omega_0 &= v(\eta q_z \pm \sqrt{q_x^2 + q_z^2}), \\ q_x &= \frac{\omega \sin \theta}{c}, \quad -\tan \theta' = q_x/q_z. \end{aligned} \quad (16)$$

The above equations may have multiple solutions or no solution. The latter signifies no refraction through the Dirac point, or that such a Dirac point cannot be excited by light from air even with the surface grating. For the case with multiple solutions, only the solutions with group velocity along z direction $v_z < 0$ delivers the refraction beam where

$$v_z = v \left(\eta \pm \frac{q_z}{\sqrt{q_x^2 + q_z^2}} \right). \quad (17)$$

From the above equation we find that for $\eta > 1$, refraction through the Dirac point is forbidden, since both branches have positive velocity. On the other hand, for $\eta < -1$, there are two solutions for Eq. (16) [see Fig. 7(b) for the number of refractive beams for various η and frequency when the incident angle is $\theta = 50^\circ$]. Indeed we observe birefringence as shown in Fig. 7(a). The two angles θ'_1 and θ'_2 as a function of frequency is shown in Fig. 7(c) for incident angle $\theta = 50^\circ$, $\omega_0 = 0.5 \frac{2\pi c}{a}$, and $v = 0.2c$ with c being the speed of light in vacuum. We notice that q_x can switch sign for both refractive beams. An important quantity for the refractive beams is the group velocity. In addition to the velocity along z direction, there is a velocity along x direction,

$$v_x = \pm v \frac{q_x}{\sqrt{q_x^2 + q_z^2}}, \quad \phi = -\arctan \frac{v_x}{v_z}. \quad (18)$$

We calculate the group velocities for the two refractive beams and plot their angle with the normal direction of the incident plane as ϕ_1 and ϕ_2 . We observe a rather simple relation between the two group velocity,

$$\phi_1 = -\phi_2. \quad (19)$$

We emphasize that the magnitude of the two group velocity is different, unless $\omega = \omega_0$. Because Dirac points appear in pairs with opposite η due to time-reversal symmetry. For type-II Dirac points, one of the Dirac cone cannot be excited, whereas the other one exhibits birefringence. This interesting phenomenon provides a route to valley selective physics for photonic Dirac points. We emphasize that when light is incident from the bottom surface (instead of the top surface) of the PhC, opposite valley contrast is realized, since in this geometry the refractive beams must have $v_z > 0$.

In contrast, for type-I Dirac points, excitation of the Dirac cone is possible if the incident angle is smaller than a critical angle θ_c . If $\theta < \theta_c$ there is only one refractive beam. We plot θ_c for various frequency and η in Fig. 7(d). From the figure we find that since the critical angle θ_c is the same for both negative and positive η with the same $|\eta|$ at the same frequency, type-I Dirac points have no valley contrasting in refraction.

VII. CONCLUSIONS AND DISCUSSIONS

We propose an effective methods of simulating Z_2 topological states in all-dielectric PhCs using nonsymmor-

phic symmetries. In a concrete example we show that for a tetragonal lattice with space group of $P4_2/mcm$, the screw symmetries lead to double degeneracy in high symmetry planes in the BZ. In this way, the screw symmetries play a similar role as Kramers degeneracy for spin-1/2 electronic Z_2 topological states.

Using this method, we find a number of Z_2 Dirac points on the M - A line (i.e., the common line of the doubly degenerate planes). In addition, we find Z_2 line-nodes around the Γ point for the first few photonic bands. The line-nodes emerge because of a degenerate partner switching mechanism: the degenerate partners have the opposite parities at the Γ point but have the same parity on the boundary of the BZ at $k_z = 0$ due to nonsymmorphic symmetry. There must be a line crossing when bands evolve from the Γ point to BZ boundaries. The nonsymmorphic symmetry plays a crucial role for degenerate partner switching, leading to rich bands degeneracy phenomena in the BZ.

As a consequence of Z_2 Dirac points, a pair of Fermi arcs are found on the surface of our PhC. The two Fermi arcs form a double helicoid surface states with a mirror symmetric spectrum with respect to $k_y = \pi/a$. The surface states are protected by the screw symmetry which allows double degeneracy at $k_y = \pi/a$. Remarkably, parts of the surface states are below the light-line which hence allows realization of “open cavity” on the PhC-air interface. We find that light is strongly confined around the interface due to the topological surface states, which allows ultrastrong coupling between TO-phonon in h-BN thin film and cavity photons. Such realization is feasible within current technology and has several fabrication and measurement advantages. The ultrastrong coupling system can provide an onset platform to study extreme limits in quantum optics, quantum phase transition, and quantum vacuum emission. With both strong interaction and nontrivial Berry phases, the system might host nontrivial states of matter such as interacting symmetry protected topological states[7]. In addition, TO-phonons in h-BN fall into the mid infrared frequencies, 170 meV, which is also important in manipulation of near field thermal emission[46].

We also find that type-II Dirac points can have anoma-

lous refraction properties: one of the valley is not excited, while the other valley has two refraction beams (i.e., birefringence). The two refraction beams have opposite group velocity along the interface. That is, one of them has positive refraction angle and the other one has negative refraction angle, in terms of group velocity. In fact, the two refraction angle are opposite to each other. These properties allow further study of valley physics[47, 48] in Dirac photonic systems.

ACKNOWLEDGMENTS.

Researches in Soochow University are jointly supported by the faculty start-up funding and the National Science Foundation of China (Grant nos: 61322504 and 11574226). J.H.J thanks Sajeev John for helpful discussions. Y.C and H.Y.K is supported by NSERC of Canada and Center for Quantum Materials at the University of Toronto.

Appendix A: $\vec{k} \cdot \vec{P}$ analysis of Dirac points

We use the $\vec{k} \cdot \vec{P}$ theory for photonic bands to study the low-energy Hamiltonian of the Dirac points. The photonic bands are solutions of the following eigenvalue equations

$$\nabla \times \frac{1}{\varepsilon(\vec{r})} \nabla \times \vec{h}_{n,\vec{k}}(\vec{r}) = \frac{\omega_{n,\vec{k}}^2}{c^2} \vec{h}_{n,\vec{k}}(\vec{r}), \quad (\text{A1})$$

where n is the band index and $\vec{h}_{n,\vec{k}}(\vec{r})$ is the Bloch function for the magnetic field of the electromagnetic wave. It is normalized as $\int_{u.c.} d\vec{r} \vec{h}_{n',\vec{k}}^*(\vec{r}) \vec{h}_{n,\vec{k}}(\vec{r}) = \delta_{nn'}$ with $u.c.$ denoting the unit cell (i.e., integration in a unit cell). The Hermitian operator $\nabla \times \frac{1}{\varepsilon(\vec{r})} \nabla \times$ is then regarded as the “photonic Hamiltonian”.

The $\vec{k} \cdot \vec{P}$ theory is constructed by expanding the Bloch functions of photonic bands near the Dirac point with the Bloch functions at the Dirac point. Direct calculation yields, the following $\vec{k} \cdot \vec{P}$ Hamiltonian,

$$\mathcal{H}_{nn'}(\vec{k}) = \frac{\omega_{n,0}^2}{c^2} \delta_{nn'} + \vec{q} \cdot \vec{P}_{nn'} - \int_{u.c.} \frac{d\vec{r}}{\varepsilon(\vec{r})} \vec{h}_{n,0}^*(\vec{r}) \cdot [\vec{q} \times (\vec{q} \times \vec{h}_{n',0}(\vec{r}))], \quad (\text{A2})$$

where $\omega_{n,0}$ is the eigen-frequency of the n^{th} band at the Dirac point. The matrix element of \vec{P} is given by

$$\vec{P}_{nn'} = \int_{u.c.} \frac{d\vec{r}}{\varepsilon(\vec{r})} [\vec{h}_{n',0}(\vec{r}) \times (i\nabla \times \vec{h}_{n,0}^*(\vec{r})) + (i\nabla \times \vec{h}_{n',0}(\vec{r})) \times \vec{H}_{n,0}^*(\vec{r})]. \quad (\text{A3})$$

A crucial fact is that the matrix element $\vec{P}_{nn'}$ is nonzero only when the n and n' bands are of different parity. In our system the mirror planes are $y = x$, $y = -x$, and $z = 0.25$. Therefore, we shall calculate the two momentum matrix elements, $\hat{P}_1 = (\hat{P}_x + \hat{P}_y)/\sqrt{2}$ and $\hat{P}_2 = (-\hat{P}_x + \hat{P}_y)/\sqrt{2}$.

We calculate the \vec{P} matrix element for the second Dirac point at $k_z > 0$. The matrix form (band index goes from

3 to 6) gives (in arbitrary units),

$$\hat{P}_1 = \begin{pmatrix} 0 & 0 & 0 & 0 \\ 0 & 0 & -0.35 - 0.26i & -0.40 + 1.61i \\ 0 & -0.35 + 0.26i & 0 & 0 \\ 0 & -0.40 - 1.61i & 0 & 0 \end{pmatrix},$$

$$\hat{P}_2 = \begin{pmatrix} 0 & 0 & 1.65 + 0.04i & 0.16 + 0.4i \\ 0 & 0 & 0 & 0 \\ 1.65 - 0.04i & 0 & 0 & 0 \\ 0.16 - 0.4i & 0 & 0 & 0 \end{pmatrix}, \quad \hat{P}_z = \begin{pmatrix} -0.74 & 0 & 0 & 0 \\ 0 & -0.74 & 0 & 0 \\ 0 & 0 & 1.5 & 0 \\ 0 & 0 & 0 & 1.5 \end{pmatrix}. \quad (\text{A4})$$

The $\vec{k} \cdot \vec{P}$ Hamiltonian in the \vec{k} linear order is then

$$\mathcal{H} = q_1 \hat{P}_1 + q_2 \hat{P}_2 + q_z \hat{P}_z, \quad (\text{A5})$$

where $q_1 = (q_x + q_y)/\sqrt{2}$ and $q_2 = (-q_x + q_y)/\sqrt{2}$, $q_x = k_x - \pi/a$, $q_y = k_y - \pi/a$, and $q_z = k_z - k_{DP}$. The above Hamiltonian faithfully restore the characteristics of the Dirac point: (i) There are two doublets for each \vec{q} [up to numerical error $\mathcal{O}(0.01)$]. (ii) Interaction is finite only between states of opposite parity. That is, the first two states have opposite parity with the other two states. Therefore, the above Hamiltonian describes a Z_2 Dirac point.

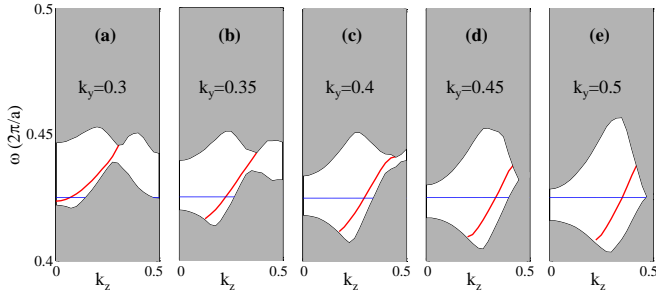


FIG. 9. (Color online) (a)-(e) Projected bulk bands (gray) and surface spectrum (red curves) vs. k_z for different k_y . All k_z and k_y are in units of $2\pi/a$. The blue line indicate the frequency $\omega = 0.425 \frac{2\pi c}{a}$.

Appendix B: Calculation of Fermi arcs associated with Z_2 Dirac points

To calculate the Fermi arcs, we set a supercell with seven periods of PhC stacked along x direction. At the two sides of the PhC is an effective medium with $\varepsilon = 0.2$. This gives an effective refractive index $n = 0.45$ which promotes the light-line to higher frequency. This technique is to ensure all the surface states of interest is confined to the surface. Without this treatment a portion of surface states is above light-line and are not confined to the surface any more. In this set-up the S_y symmetry is kept by using an odd number of unit cells in the supercell calculation. This is crucial to keep the double degeneracy on the $k_y = \pi/a$ line in the surface BZ.

The Fermi arcs are obtained by scanning the surface BZ. Specifically, for a series of k_y points, we calculate the projected bulk bands, as well as the spectrum of the surface states. The latter is obtained by comparing the spectrum of the supercell and the projected bulk bands.

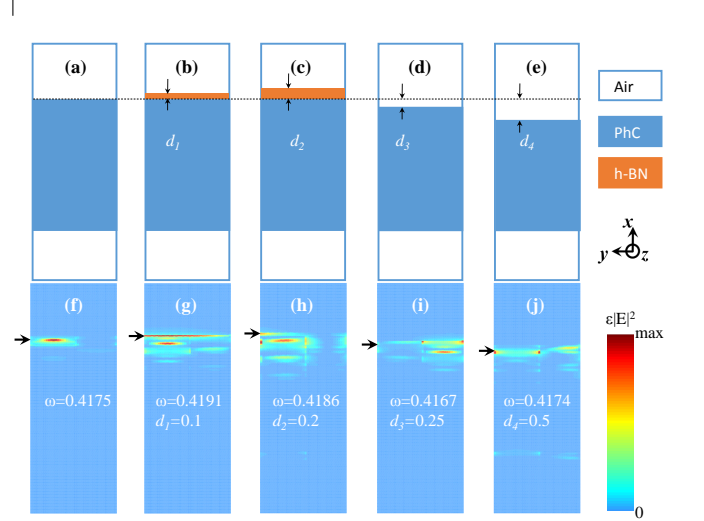


FIG. 10. (Color online) (a)-(e): Schematic of various supercell to calculate the surface states. (a) Seven periods of PhC stacking along the x direction and $3a$ thick air layers above and below the PhC. (b): With a layer of h-BN on the PhC surface of thickness $0.1a$. The dielectric constant of h-BN is taken as 8. (c): With a h-BN layer of thickness $0.2a$. (d) When the surface layer of PhC is cut by $0.25a$. (e) When the surface layer of PhC is cut by $0.5a$. (f)-(j): Frequency and profile of $\varepsilon|\vec{E}|^2$ (integrated over z direction) in the x - y plane. The arrows indicate the position of the interfaces. The wavevector of the surface state is $\vec{k} = (0, 0.5, -0.3) \frac{2\pi}{a}$.

The states lie in the projected band gap is identified as the surface states. We show in Fig. 9 the spectrum of the projected bulk bands (gray) and surface states (red). The Fermi arc is obtained via finding the \vec{k} points in the surface BZ with the given frequency (i.e., the intersection between the red curve and the blue line).

Appendix C: Robustness of topological states

To demonstrate the robustness of the topological surface states we calculate the surface states for various modification of the structure. In Fig. 10 we compare the frequency and field profile $\epsilon|\vec{E}|^2$ for the supercell with

no modification (a), the supercell with h-BN on top of the surface of different thickness (b) and (c), and the supercell with the surface layer cut by $0.25a$ and $0.5a$ (e) and (f). We find that the frequency of the surface states for various situations are very close. The energy density is focused on the surface for various situations. Those observations indicate the robustness of the topological surface states.

-
- [1] M. Z. Hasan and C. L. Kane, *Topological Insulators*, Rev. Mod. Phys. **82**, 3045-3067 (2010).
- [2] X.-L. Qi and S.-C. Zhang, *Topological insulators and superconductors*, Rev. Mod. Phys. **83**, 1057-1110 (2011)
- [3] O. Vafek and A. Vishwanath, *Dirac Fermions in Solids: From High-Tc Cuprates and Graphene to Topological Insulators and Weyl Semimetals*, Ann. Rev. Condens. Matt. Phys. **5**, 83 (2014).
- [4] Y. Chen, Y.-M. Lu, and H.-Y. Kee, *Topological Crystalline Metal in Orthorhombic Perovskite Iridates*, Nat. Commun. **6**, 6593 (2015).
- [5] Y. Chen, H.-S. Kim, and H.-Y. Kee, *Topological crystalline semimetals in non-symmorphic lattices*, Phys. Rev. B **93**, 155140 (2016)
- [6] X. G. Wen, *Quantum Field Theory of Many-Body Systems* (Oxford University Press, Oxford, 2004)
- [7] X. Chen, Z.-C. Gu, Z.-X. Liu, and X.-G. Wen, *Symmetry Protected Topological Orders in Interacting Bosonic Systems*, Science **338**, 1604-1606 (2012).
- [8] A. Chutinan, S. John, and O. Toader, *Diffractionless Flow of Light in All-Optical Micro-chips*, Phys. Rev. Lett. **90**, 123901 (2003).
- [9] F. D. M. Haldane and S. Raghu, *Possible realization of directional optical waveguides in photonic crystals with broken time-reversal symmetry*, Phys. Rev. Lett. **100**, 013904 (2008).
- [10] Z. Wang, Y. D. Chong, J. D. Joannopoulos, and M. Soljačić, *Reflection-free one-way edge modes in a gyromagnetic photonic crystal*, Phys. Rev. Lett. **100**, 013905 (2008).
- [11] M. Hafezi, E. A. Demler, M. D. Lukin, J. M. Taylor, *Robust optical delay lines with topological protection*, Nat. Phys. **7**, 907 (2011).
- [12] I. Söllner et al., *Deterministic photon-emitter coupling in chiral photonic circuits*, Nat. Nanotech. **10**, 775 (2015).
- [13] M. D. Turner, M. Saba, Q. Zhang, B. P. Cumming, G. E. Schröder-Turk, and M. Gu, *Miniature chiral beamsplitter based on gyroid photonic crystals*, Nat. Photon. **7**, 801 (2013)
- [14] Z. Wang, Y. Chong, J. D. Joannopoulos, and M. Soljačić, *Observation of unidirectional backscattering-immune topological electromagnetic states*, Nature (London) **461**, 772 (2009).
- [15] M. Hafezi, S. Mittal, J. Fan, A. Migdall, and J. Taylor, *Imaging topological edge states in silicon photonics*, Nat. Photon. **7**, 1001 (2013).
- [16] L. Lu, L. Fu, J. D. Joannopoulos, and M. Soljačić, *Weyl points and line nodes in gyroid photonic crystals*, Nat. Photon. **7**, 294 (2013).
- [17] M. C. Rechtsman, J. M. Zeuner, Y. Plotnik, Y. Lumer, D. Podolsky, F. Dreisow, S. Nolte, M. Segev, and A. Szameit, *Photonic Floquet topological insulators*, Nature **496**, 196 (2013).
- [18] X. Huang, Y. Lai, Z. H. Hang, H. Zheng, and C. T. Chan, *Dirac cones induced by accidental degeneracy in photonic crystals and zero-refractive-index materials*, Nat. Mater. **10**, 582 (2011).
- [19] A. B. Khanikaev, S. H. Mousavi, W.-K. Tse, M. Kargarian, A. H. MacDonald, and G. Shvets, *Photonic topological insulators*, Nat. Mater. **12**, 233 (2013).
- [20] W.-J. Chen, S.-J. Jiang, X.-D. Chen, J.-W. Dong, and C. T. Chan, *Experimental realization of photonic topological insulator in a uniaxial metacrystal waveguide*, Nat. Commun. **5**, 5782 (2014).
- [21] L.-H. Wu and X. Hu, *Scheme for Achieving a Topological Photonic Crystal by Using Dielectric Material*, Phys. Rev. Lett. **114**, 223901 (2015).
- [22] C. He, X.-C. Sun, X.-P. Liu, M.-H. Lu, Y. Chen, L. Feng, and Y.-F. Chen, *Photonic topological insulator with broken time-reversal symmetry*, Proc. Natl. Acad. Sci. USA **113**, 4924 (2016).
- [23] H.-X. Wang, L. Xu, H.-Y. Chen, and J.-H. Jiang, *Three-dimensional photonic Dirac points stabilized by point group symmetry*, Phys. Rev. B **93**, 235155 (2016).
- [24] W. Gao, B. Yang, M. Lawrence, F. Fang, B. Béni, and S. Zhang, *Plasmon Weyl Degeneracies in Magnetized Plasma*, arXiv:1511.04875
- [25] L. Lu, J. D. Joannopoulos, and M. Soljačić, *Topological photonics*, Nat. Photon. **8**, 821 (2014).
- [26] M. Xiao, Z. Q. Zhang, and C. T. Chan, *Surface Impedance and Bulk Band Geometric Phases in One-Dimensional Systems*, Phys. Rev. X **4**, 021017 (2014).
- [27] L. Lu, Z. Wang, D. Ye, L. Ran, L. Fu, J. D. Joannopoulos, and M. Soljačić, *Experimental observation of Weyl points*, Science **349**, 622 (2015).
- [28] W.-J. Chen, M. Xiao, and C. T. Chan, *Experimental observation of robust surface states on photonic crystals possessing single and double Weyl points*, arXiv:1512.04681
- [29] M. Hafezi, *Measuring Topological Invariants in Photonic Systems*, Phys. Rev. Lett. **112**, 210405 (2014).
- [30] S. Mittal, S. Ganeshan, J. Fan, A. Vaezi, and M. Hafezi, *Measurement of topological invariants in a 2D photonic system*, Nat. Photon. **10**, 180 (2016).
- [31] L. Lu, C. Fang, L. Fu, S. G. Johnson, J. D. Joannopoulos, and M. Soljačić, *Symmetry-stabilized topological photonic crystal in three dimensions*, Nat. Phys. **12**, 337 (2016).
- [32] I. Carusotto and C. Ciuti, *Quantum fluids of light*, Rev. Mod. Phys. **85**, 299 (2013).
- [33] T. Niemczyk et al., *Circuit quantum electrodynamics in the ultrastrong-coupling regime*, Nat. Phys. **6**, 772 (2010).

- [34] Y. Todorov, A. M. Andrews, R. Colombelli, S. De Liberato, C. Ciuti, P. Klang, G. Strasser, and C. Sirtori, *Ultrastrong Light-Matter Coupling Regime with Polariton Dots*, Phys. Rev. Lett. **105**, 196402 (2010).
- [35] G. Scalari et al., *Ultrastrong Coupling of the Cyclotron Transition of a 2D Electron Gas to a THz Metamaterial*, Science **335**, 1323 (2012).
- [36] D. Hagenmüller and C. Ciuti, *Cavity QED of the Graphene Cyclotron Transition*, Phys. Rev. Lett. **109**, 267403 (2012).
- [37] S. De Liberato, C. Ciuti, and I. Carusotto, *Quantum Vacuum Radiation Spectra from a Semiconductor Microcavity with a Time-Modulated Vacuum Rabi Frequency*, Phys. Rev. Lett. **98**, 103602 (2007).
- [38] B.-J. Yang, T. Morimoto, and A. Furusaki, *Topological charges of three-dimensional Dirac semimetals with rotation symmetry*, Phys. Rev. B **92**, 165120 (2015).
- [39] J.-H. Jiang, *Tunable topological Weyl semimetal from simple-cubic lattices with staggered fluxes*, Phys. Rev. A **85**, 033640 (2012).
- [40] Z. Wang, Y. Sun, X.-Q. Chen, C. Franchini, G. Xu, H. Weng, X. Dai, and Z. Fang, *Dirac semimetal and topological phase transitions in A_3Bi ($A=Na, K, Rb$)*, Phys. Rev. B **85**, 195320 (2012).
- [41] C. Fang, L. Lu, J. Liu, and L. Fu, *Topological semimetals with helicoid surface states*, arXiv:1512.01552, Nat. Phys. in press.
- [42] J.-H. Jiang and S. John, *Photonic Crystal Architecture for Room-Temperature Equilibrium Bose-Einstein Condensation of Exciton Polaritons*, Phys. Rev. X **4**, 031025 (2014).
- [43] J.-H. Jiang and S. John, *Photonic Architectures for Equilibrium High-Temperature Bose-Einstein Condensation in Dichalcogenide Monolayers*, Sci. Rep. **4**, 7432 (2014).
- [44] R. Geick, C. H. Perry, and G. Rupprecht, *Normal Modes in Hexagonal Boron Nitride*, Phys. Rev. **146**, 543 (1966).
- [45] A. Ridolfo, M. Leib, S. Savasta, and M. J. Hartmann, *Photon Blockade in the Ultrastrong Coupling Regime*, Phys. Rev. Lett. **109**, 193602 (2012).
- [46] Y. Guo, C. L. Cortes, S. Molesky, and Z. Jacob, *Broadband super-Planckian thermal emission from hyperbolic metamaterials*, Appl. Phys. Lett. **101**, 131106 (2012).
- [47] K. F. Mak, K. He, J. Shan, and T. F. Heinz, *Control of valley polarization in monolayer MoS₂ by optical helicity*, Nat. Nanotech. **7**, 494 (2012).
- [48] Q.-D. Jiang, H. Jiang, H. Liu, Q.-F. Sun, and X. C. Xie, *Topological Imbert-Fedorov shift in Weyl semimetals*, Phys. Rev. Lett. **115**, 156602 (2015).